Integrated lithium niobate microwave photonic processing engine

Hanke Feng[1], Tong Ge[1], Xiaoqing Guo[1,2], Sha Zhu[1,3], Ke Zhang[1], Yiwen Zhang[1], Zhaoxi Chen[1], Wenzhao Sun[1,4,5], Yixuan Yuan[1,6] and Cheng Wang[1*]

[1]*Department of Electrical Engineering & State Key Laboratory of Terahertz and Millimeter Waves, City University of Hong Kong, Kowloon, Hong Kong, China*
[2]*Department of Engineering Science, University of Oxford, Oxford, UK*
[3]*College of Microelectronics, Faculty of Information Technology, Beijing University of Technology, Beijing, China*
[4]*City University of Hong Kong (Dongguan), Dongguan, China*
[5]*Center of Information and Communication Technology, City University of Hong Kong Shenzhen Research Institute, Shenzhen, China*
[6]*Department of Electronic Engineering, Chinese University of Hong Kong, Shatin, Hong Kong, China*
*cwang257@cityu.edu.hk

Abstract: Integrated microwave photonics (MWP) is an intriguing field that leverages integrated photonic technologies for the generation, transmission, and manipulation of microwave signals in chip-scale optical systems [1,2]. In particular, ultrafast processing and computation of analog electronic signals in the optical domain with high fidelity and low latency could enable a variety of applications such as MWP filters [3-5], microwave signal processing [6-9], and image recognition [10,11]. An ideal photonic platform for achieving these integrated MWP processing tasks shall simultaneously offer an efficient, linear and high-speed electro-optic (EO) modulation block to faithfully perform microwave-optic conversion at low power, and a low-loss functional photonic network that can be configured for a variety of signal processing tasks, as well as large-scale, low-cost manufacturability to monolithically integrate the two building blocks on the same chip. In this work, we demonstrate such an integrated MWP processing engine based on a thin-film lithium niobate (LN) platform capable of performing multi-purpose processing and computation tasks of analog signals up to 92 giga samples per second (GSa/s) at CMOS-compatible voltages. By integrating a high-speed EO modulation block and a multi-purpose low-loss signal processing section on the same chip fabricated from a 4-inch wafer-scale process, we demonstrate high-speed analog computation, i.e., first- and second-order temporal integration and differentiation with

computing accuracies up to 98.1 %, and deploy these functions to showcase three proof-of-concept applications, namely, ordinary differential equation (ODE) solving, ultra-wideband (UWB) signal generation and high-speed edge detection of images. We further leverage the image edge detector to enable a photonic-assisted image segmentation model that could effectively outline the boundaries of melanoma lesion in medical diagnostic images, achieving orders of magnitude faster processing speed and lower power consumption than conventional electronic processors. Our ultrafast LN MWP engine could provide compact, low-power, low-latency, and cost-effective solutions for future wireless communications, internet of things, high-resolution radar systems and photonic artificial intelligence.

Main

The rapid expansion of wireless networks and Internet of Things (IoTs), cloud-based services is posing pressing challenges on the electronic bandwidth, power consumption, and performance of underlying radio frequency (RF) systems [12]. The ever-growing artificial intelligence (AI) technologies also demand ultrahigh-speed, low-power, and low-latency processing and computation of analog signals much beyond those offered by traditional electronic integrated circuits. Microwave photonics (MWP) provides effective solutions to address these challenges through the usage of optical devices to perform microwave signal generation, transmission and manipulation tasks [1]. Recently, the surge of photonic integration technologies has further led to a dramatic reduction in the size, weight, and power (SWaP) of MWP systems with enhanced robustness and functionalities, termed integrated MWP [2]. Impressive demonstrations of integrated MWP applications include arbitrary RF waveform generation [13,14], true-time delay beamforming [15], instantaneous frequency measurement [16] and so on.

Despite the tremendous progress, integrated MWP systems still face substantial challenges in performing ultrahigh-speed analog signal processing tasks with chip-scale integration, high fidelity, and low power at the same time. An ideal photonic platform to meet these demands should support electro-optic (EO) modulators with low drive voltages, broad bandwidths and high linearity to faithfully convert microwave signals into optical signals, as well as a versatile low-loss functional device toolbox for further processing the converted signals in the optical domain. To date, most MWP applications have been demonstrated in silicon photonics [7,8,13,14,16] owing to its low-cost, large-scale fabrication readiness and the wide availability of functional devices. However, the free carrier injection-based modulation mechanism [17] in silicon is intrinsically accompanied with nonlinear EO response, large carrier-absorption loss, limited response speed, and low power-handling ability, resulting in critical trade-offs between the signal fidelity, power consumption and operation bandwidth

3

achievable in silicon MWP systems. Indium phosphide (InP) is another attractive platform for MWP systems with potential for monolithic integration of active and passive photonic elements on the same chip [4,6]. However, the relatively large propagation loss and small index contrast in InP waveguides [2], together with yield issues, significantly hurdle the performances and functionalities achievable in the signal processing section of future large-scale MWP systems. While silicon nitride (SiN) [18,19] is an excellent MWP platform by virtue of its ultra-low propagation loss and high-power handling ability, the lack of second-order nonlinearity prevents the realization of high-speed EO modulators in a monolithic SiN platform.

As a result of these material trade-offs, many integrated MWP systems have been realized by combining silicon or SiN photonic chips with traditional off-the-shelf lithium niobate (LN) modulators, enabling advanced computation and information processing tasks, such as differentiation, integration and Hilbert transformation [20-25], at the expense of increased bulkiness, system complexity and power consumption. Such signal processing and computation have also been demonstrated in all-optical circuits [6,26,27], offering potential processing bandwidths up to several THz [27]. However, the processed signals in these demonstrations are usually limited to simple Gaussian or Gaussian-derived waveforms generated by contemporary all-optical techniques, e.g., mode-locked lasers, while signals urgently in need of high-speed processing capability today are often much more complicated and arbitrary and can only be accessed from the electronic domain. Another potential solution is heterogeneous technology [16,28-30] that integrates III-V lasers/photodetector and silicon modulators with low-loss SiN passive photonics via hetero-epitaxial growth or wafer bonding, while with additional cost and complexity in fabrication.

The recently emerged thin-film lithium niobate (LN) platform is a promising candidate to address these urgent demands and critical challenges by integrating efficient EO convertors and low-loss signal processors on the same chip [31]. The Pockels effect in LN is intrinsically linear, instantaneous and low-loss, ideally suited for

4

realizing high-fidelity microwave-optic signal conversion with low power consumption and broad bandwidths [32]. Recently, many miniaturized and high-performance LN modulators have been demonstrated, exhibiting bandwidths covering the entire microwave and millimeter-wave bands [33-35], CMOS-compatible drive voltages [36,37], and ultra-high linearity performance[38]. Moreover, a full range of high-performance and low-loss functional devices are now endowed on the same platform, including ultrahigh-Q microresonators [39], programmable filters [40], efficient frequency converters/shifters [41] as well as low-loss delay lines [42]. Efforts to scale up these elements into LN photonic integrated circuits (PIC) with low propagation loss and wafer-scale manufacturability has recently further boosted the cost effectiveness and commercial relevance towards a potentially high-performance, large-scale, and multi-purpose LN MWP system [43,44].

Here, we fulfill this promise by demonstrating a high-fidelity, broadband and low-power-consumption MWP system leveraging a 4-inch wafer-scale LN platform, realizing high-speed analog computation of electronic signals up to 92 GSa/s with multi-purpose functionalities, i.e., first- and second-order temporal integration and differentiation. Building upon these computation functions, we show three proof-of-concept applications, including ordinary differential equation (ODE) solving, ultra-wide bandwidth (UWB) signal generation, and high-speed edge-feature detection of images. Furthermore, we plug the photonics-assisted image-edge detector, with orders of magnitude higher computing speed and lower power consumption than traditional electronics-based image-edge detection algorithms, into a neural network-based image segmentation model [45] and showcase the effective identification of melanoma lesion outlines in medical diagnostic images.

Results

Figure 1 shows the schematic illustration of our multi-purpose MWP system on LN platform, consisting of an efficient EO modulation section for transferring high-speed microwave signals into optical domain, and a low-loss signal processing section for realizing the analog computation functions, including first- and second-order

temporal integration and differentiation. The PICs are directly patterned on a 4-inch thin-film LN wafer as shown in the background of Fig. 1 using an ultraviolet (UV) stepper lithography system (see Methods). Our LN MWP platform supports a variety of high-performance device building blocks, including microring resonators with high intrinsic quality (Q) factors > 4 million (corresponding to propagation loss < 0.1 dB/cm), broadband low-voltage intensity/phase modulators, add-drop microring resonators as temporal integrators, unbalanced Mach-Zehnder interferometers (MZIs) as differentiators, as well as respective cascaded versions for second-order integration and differentiation tasks. The corresponding microscope images of these photonic building blocks and their measured critical performance metrics are shown in the top and bottom insets of Fig. 1. Side insets of Fig. 1 show the false-colored scanning electron microscope images of the waveguide sidewall, the coupling region of a microresonator, the cross-section of a waveguide, and a multi-mode interference (MMI) coupler, respectively. More details on the device design and fabrication can be found in methods. Based on these MWP building blocks, we next discuss two ultrahigh-speed microwave signal computation processes, i.e. temporal integration and differentiation, as well as their applications.

High-speed microwave photonic temporal integrator

Figure 2a illustrates the working principle of our high-speed MWP temporal integrator, which consists of an MZI amplitude modulator and add-drop ring resonators, and is designed to take the temporal integration of a complex input microwave signal and output in the form of optical intensity (see methods). An integration task in the time domain is equivalent to a transfer function of $H(\omega) = \frac{1}{j(\omega-\omega_0)}$ in the frequency domain [26], where $j = \sqrt{-1}$, ω is the optical angular frequency and ω_0 is the carrier frequency of the signal to be processed. Here we adopt add-drop ring resonators to serve as integrators [6,22,26], where the Lorentzian lineshape approximately follows the above transfer function within the resonance bandwidth, as shown in Fig. 2c.
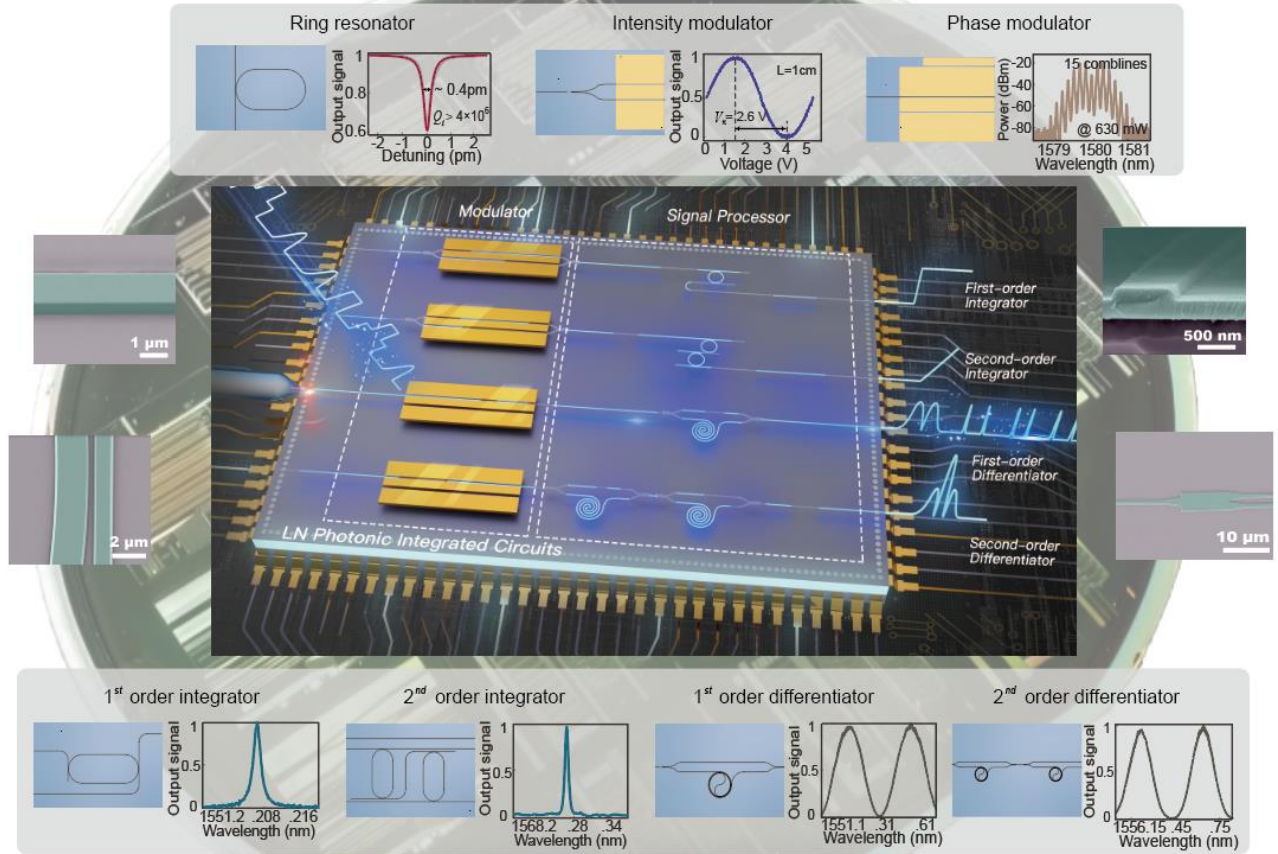
Fig. 1. Wafer-scale LN-based MWP signal processing engine and building blocks. The MWP processing engine, as schematically illustrated in the middle panel, consists of a high-speed EO modulation section that faithfully converts analog electronic signals into optical domain, and a low-loss multi-purpose photonic processing section. Top and bottom rows show the microscope images and key performance metrics of the fundamental building blocks of our high-speed MWP systems, including micro-resonators with intrinsic quality factors $> 4 \times 10^6$, low-voltage intensity and phase modulators for signal encoding, add-drop ring resonators as integrators, unbalanced MZIs as differentiators, as well as cascaded rings and MZIs as second-order integrators and differentiators. The LN MWP integrated circuits are fabricated on a 4-inch wafer scale using a UV stepper lithography system. Background of the figure shows a photograph of the processed wafer, whereas the left and right insets are detailed false-color scanning electron micrographs (SEM) of the devices, showing the sidewall of a waveguide, the coupling region of a micro-resonator, the cross-section view of a waveguide and a multi-mode interference (MMI) coupler, respectively.

This first-order integrator has a measured free spectral range (FSR) of 80 GHz, a loaded Q factor of ~ 0.9

million measured at the drop port, which corresponds to a photon lifetime of 700 ps (Fig. 1c). We characterize

the performance of our LN-based MWP integrator using the experimental setup shown in Fig. 2b. Notably,

the measurements are performed using signals directly generated from an arbitrary-waveform generator

without the use of microwave amplifiers (peak voltage = 500 mV), enabled by the low-driving voltage and high signal-to-noise ratio of our LN modulators, promising for future low-power-consumption and high-fidelity MWP systems. The integration results in the form of optical intensity are recorded by a high-speed photodetector (PD) through homodyne detection with the optical carrier itself when the modulator is biased at the quadrature point. (see methods)

We first test the basic performance of our first-order integrator by injecting a Gaussian pulse with a full width at half maximum (FWHM) of 90 ps. The output signals in Fig. 2e (*i*) clearly show a step-like waveform with an integration time up to ~ 600 ps (defined as the decay time to reach 80 % of the maximum intensity [26]), consistent with our resonator lifetime. Using resonators with even higher *Q*-factors could further increase the integration time, at the expense of lower throughput due to narrower resonance linewidths (or operation bandwidths) [6]. Next, we demonstrate coherent integration of more advanced waveforms by injecting in-phase (*ii*) and out-of-phase (*iii*) doublet pulses, as well as triplet pulses (*iv*), the corresponding results of which are shown in Fig. 2e. Specifically, the results for the in-phase doublet pulses (*ii*) feature a clear double-step function due to the constructive addition of the two waveforms, and the duration time of the step profile matches the interval between the two pulses. Such functions could potentially find applications in high-speed bit counting. In contrast, when the two pulses are out of phase (*iii*), the time integral of the second optical pulse cancels with that of the first one, leading to a rapid return to the baseline. Different duration time can be readily obtained by setting the position of the second pulse to realize the signal memory function [46]. We then input a more complex triplet pulse (*iv*) to verify the capability of processing complicated RF signals, the result of which shows an average accuracy of 96.06% compared with the simulated output. Based on the results of the first-order temporal integrator, we further demonstrate second-order integration function by cascading two microring resonators with aligned resonance peaks (Fig. 2d) (see methods). When injecting a

8

single Gaussian pulse (FWHM ~ 120 ps), the corresponding output (Fig. 2e, v) matches well with the

simulation prediction, with an average accuracy of 96.03 % within the device lifetime, and shows a much

longer rise time than the duration of the input pulse, indicating the effective realization of second-order

integration function.

We then apply this integrator to showcase our first MWP application, i.e. solving ordinary differential

equations (ODE) for high-speed electronic signals, expressed as: $\frac{dy(t)}{dt} + ky(t) = x(t)$, where $x(t)$ represents

the input RF signal, $y(t)$ is the solution to be determined, and k represents an arbitrary constant [22]. This basic

ODE can be utilized to model a broad range of basic engineering systems and physical phenomena, such as

temperature diffusion processes and automatic control systems [22,47]. The process of solving this ODE in the

time domain could be described canonically as an integration function embedded inside a feedback loop,

which is equivalent to a Lorentzian transfer function of $H(\omega) = \frac{1}{j(\omega-\omega_0)+k}$ in the frequency domain (Fig. 2f).

We achieve this transfer function again using an add-drop ring resonator, where the loaded Q factor determines

the constant k in the ODE [22](see methods). As a proof of concept, we fabricate and test three different ring

resonators with Q factors of 4.8×10^5, 1.7×10^5, and 0.8×10^5 by controlling the coupling gaps (Fig. 2g),

corresponding to k values of 1.24 ns⁻¹, 3.49 ns⁻¹ and 7.44 ns⁻¹, respectively. During the testing, we use 400 ps

super-Gaussian pulses as input signals to better distinguish the solutions from the input [47]. The respective

results with different k constants in Fig. 2h show excellent agreement with simulated solutions (dashed lines)

obtained by an ideal ODE solver, with an average computation accuracy of 98.1 %. Compared with algorithms

in traditional electronics that require multiple iterations, our MWP system solves the ODE almost

instantaneously as photons pass through, significantly improving the processing speed while maintaining

excellent computation accuracy. Further equipping the resonators with thermo-optic or EO tunable couplers

to actively control the loaded Q factor could enable a tunable ODE solver with variable coefficients to address

more complex practical application scenarios [48].
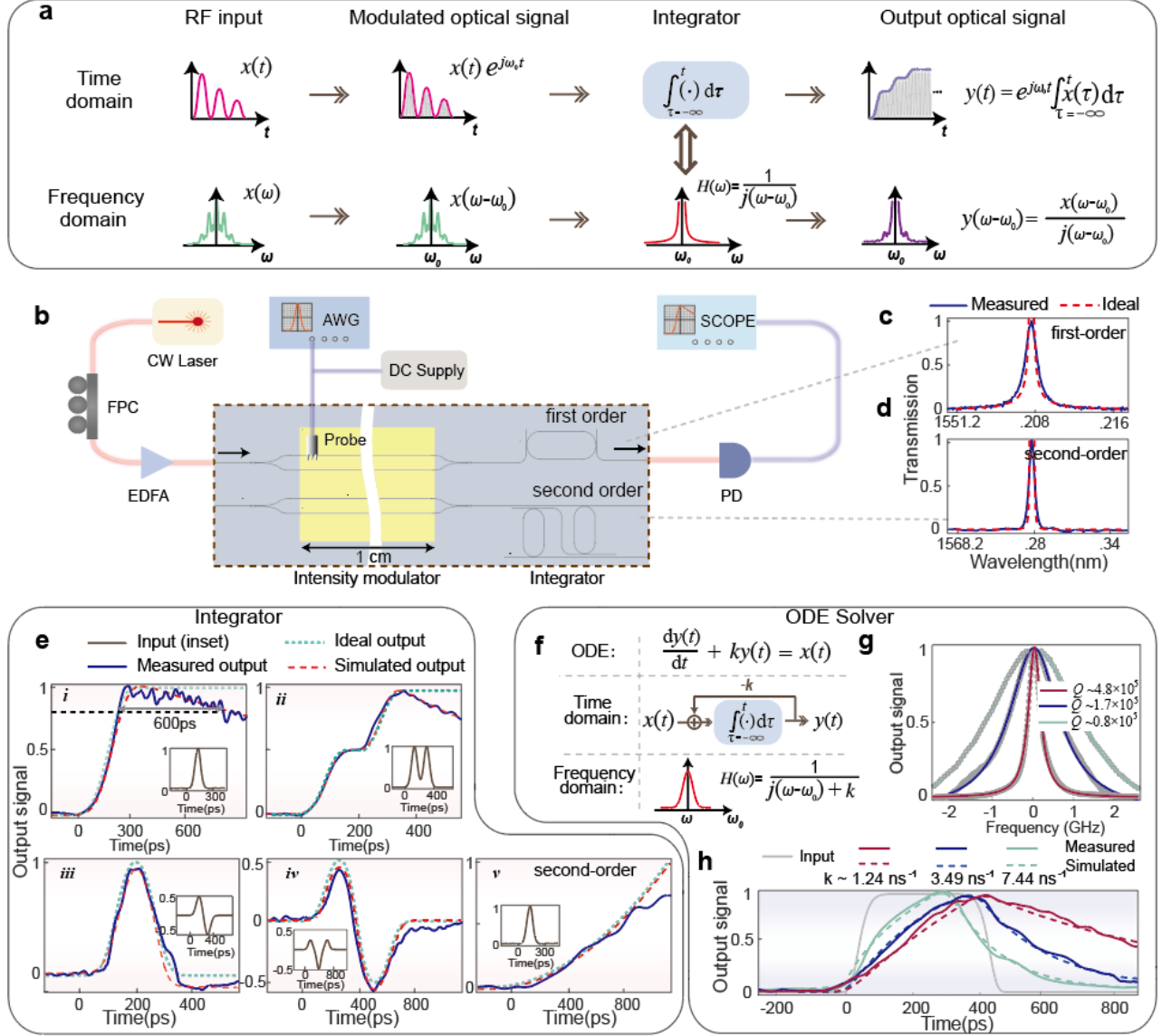
Fig. 2. High-speed microwave photonic temporal integrator. a. Working principle of our MWP temporal integrator. An integration task in the time domain is equivalent to a transfer function of $H(\omega) = 1/j(\omega - \omega_0)$ in the frequency domain. **b.** Experimental setup for the measurement of the MWP integrator. Inset shows a microscope image of the device. AWG, arbitrary waveform generator; FPC, fiber polarization controller; EDFA, Erbium-doped fiber amplifier; PD, photodetector. **c, d.** Measured (solid) and ideal (dashed) transfer functions for the first- and second-order integrators. **e.** Normalized measured temporal responses of the integrator (blue solid), together with simulated (red dashed) and ideal (green dotted) responses, for (*i*) first-order integration of a single Gaussian pulse showing an integration time of 600 ps, (*ii*) first-order integration of an in-phase doublet pulse featuring a clear double-step profile, (*iii*) first-order integration of an out-of-phase doublet pulse, showing a rapid return to the baseline when the second pulse comes in, (*iv*) first-order integration of a triplet pulse, and (*v*) second-order integration of a single Gaussian pulse. Insets: the corresponding input RF waveforms. **f.** Working principle of the ordinary differential equation (ODE) solving system. **g.** Measured transfer functions of the ODE solvers with different Q factors corresponding to three different k coefficients. **h.** Normalized measured (solid) and ideal (dashed) ODE solutions of a 400-ps input super-Gaussian pulse (grey) for different k coefficients.
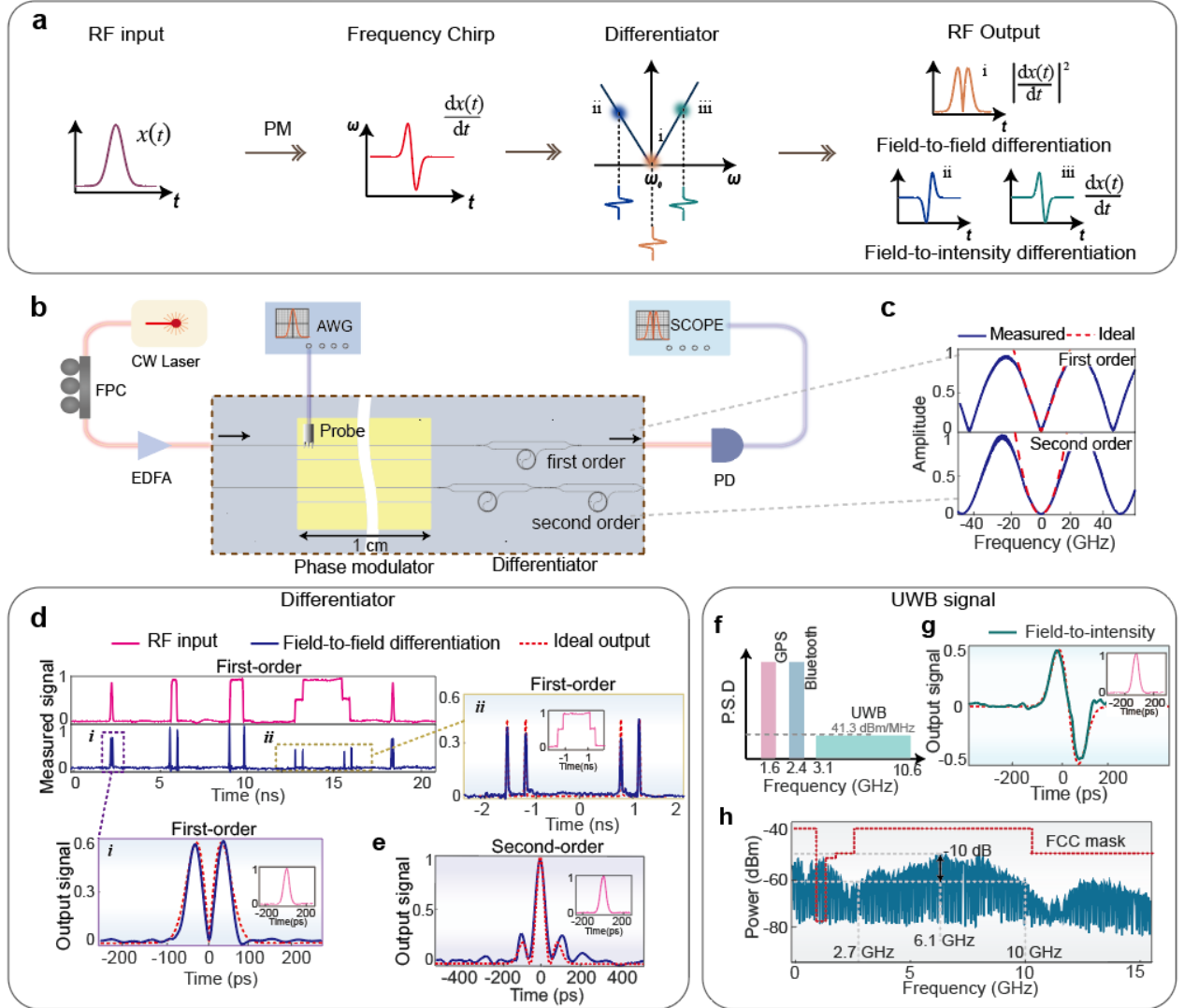
High-speed microwave photonic temporal differentiator

The second demonstrated high-speed MWP computation task is temporal differentiation, which takes the

derivative of the input microwave signal and output in the form of optical field or intensity. Here, we deploy

a frequency-chirp-based differentiation scheme [20] leveraging an EO phase modulator and an MZI-based

differentiator on the LN platform (see methods). The basic working principle is shown in Fig. 3a: the input

RF signal $x(t)$ is first loaded on a continuous-wave optical signal by the phase modulator, leading to an

instantaneous optical phase of $\omega_0 + \beta x(t)$, where ω_0 is the carrier frequency of the signal and β is the

modulation index. This induces an instantaneous frequency chirp of $\omega_0 + \beta \frac{dx(t)}{dt}$ that exactly follows the

differentiation of the input signal $\frac{dx(t)}{dt}$. The chirped frequency information is then mapped into optical field

or intensity using a signal processing unit, i.e. an unbalanced MZI, which is carefully designed to provide the

desired frequency response. Specifically, we achieve field-to-field (field-to-intensity) differentiation by

biasing the MZI at the null (quadrature) point, where the output optical field (intensity) is linearly proportional

to the optical frequency [20]. The top panel of Fig. 3c shows the measured transfer function of the fabricated

unbalanced MZI as a first-order differentiator, consistent with the ideal linear response within a processing

bandwidth of 40 GHz, limited by FSR. Even higher processing bandwidths could be achieved using MZIs

with larger FSR, however, at the expense of lowered differentiation efficiency (determined by the spectral

slope of the transfer function) [20]. We could also achieve second-order differentiation by cascading two

unbalanced MZIs will aligned null wavelengths, the transfer function of which is shown in the bottom panel

of Fig. 3c with a faithful processing bandwidth of 30 GHz.

We test the field-to-field differentiation performance by injecting a sequence of RF signals including Gaussian

pulses (FWHM ~ 90ps, 120ps), square pulses (FWHM ~ 300ps, 500ps) and stepped pulses [Fig. 3d (red)] into

the phase modulator, using the experimental setup shown in Fig. 3b. The blue trace in Fig. 3d shows the

corresponding measured output differentiation results, where the pulse height is determined by the temporal rising/falling slope of input signals. Here the output signals are positive for both rising and falling edges since the differentiation result in the form of optical field is measured by a direct intensity detection at the PD showing $\left|\frac{dx(t)}{dt}\right|^2$. The insets of Fig. 3d show blow-up views of input and output waveforms together with the ideal ones, showing an average accuracy of 96.47%. The slight mismatch is mainly originated from the limited analog bandwidth of our AWG (see methods). We further test the second-order field-to-field differentiation performance by injecting a 120-ps Gaussian pulse to the cascaded MZI device (Fig. 3e), which also shows good agreement with the expected result.

One attractive MWP application based on the differentiator is the generation of UWB signals, an emerging wireless protocol with wide bandwidth (3.1-10.6 GHz) and low power spectral density (< 41.3 dBm/MHz) for short-range high-throughput wireless communications and sensor networks [49] (Fig. 3f). Here we demonstrate the generation of UWB carrier pulses by performing field-to-intensity differentiation to Gaussian monocycle pulses (Fig. 3g) (see methods). The differentiation results in this case are carried by optical intensity and measured through a homodyne detection similar to that used in field-to-intensity integration, showing an anti-symmetric doublet pulse with an average accuracy of 97.42% compared with the ideal response. The corresponding RF spectrum of the output UWB pulse is shown in Fig. 3h, featuring a center frequency of 6.1 GHz and a 10-dB bandwidth of 7.3 GHz, with a fractional bandwidth of 120%, in accordance with the Federal Communications Commission (FCC) regulations [49]. The demonstrated UWB signal generation on our LN MWP platform could provide compact and cost-effective solutions for next-generation wireless communications and remote sensing systems with seamless compatibility with optical networks.

Fig. 3. High-speed microwave photonic temporal differentiator. a. Working principle of the frequency-chirp-based MWP temporal differentiator. Input RF signal $x(t)$ is first loaded on an optical carrier by a phase modulator to induce an instantaneous frequency chirp that follows the differentiation of the input signal. The chirped frequency information is then projected into optical field or intensity through an unbalanced MZI biased at the null or the quadrature point, respectively. **b.** Experimental setup for the measurement of MWP differentiator. Inset shows a microscope image of the device. **c.** Measured and ideal transfer functions for the first- and second-order differentiators. **d.** Measured field-to-field differentiation response (blue) for a sequence of input RF signals (red). Blow-up panels show the measured (blue solid) and ideal (red dashed) results for a Gaussian pulse (*i*) and a stepped pulse (*ii*) (see insets). **e.** Second-order field-to-field differentiation results for a Gaussian input pulse as shown in the inset. **f.** Illustration of the power spectrum density (P.S.D.) and frequency range of UWB signal compared with GPS and Bluetooth. **g.** Measured (green solid) and ideal (red dashed) UWB monocycle pulse generated by field-to-intensity differentiation of a Gaussian pulse (inset). **h.** Measured RF spectrum of the generated UWB signal from 0 to 15 GHz. Red dashed line shows the power spectrum mask regulated by Federal Communications Commission (FCC).

13

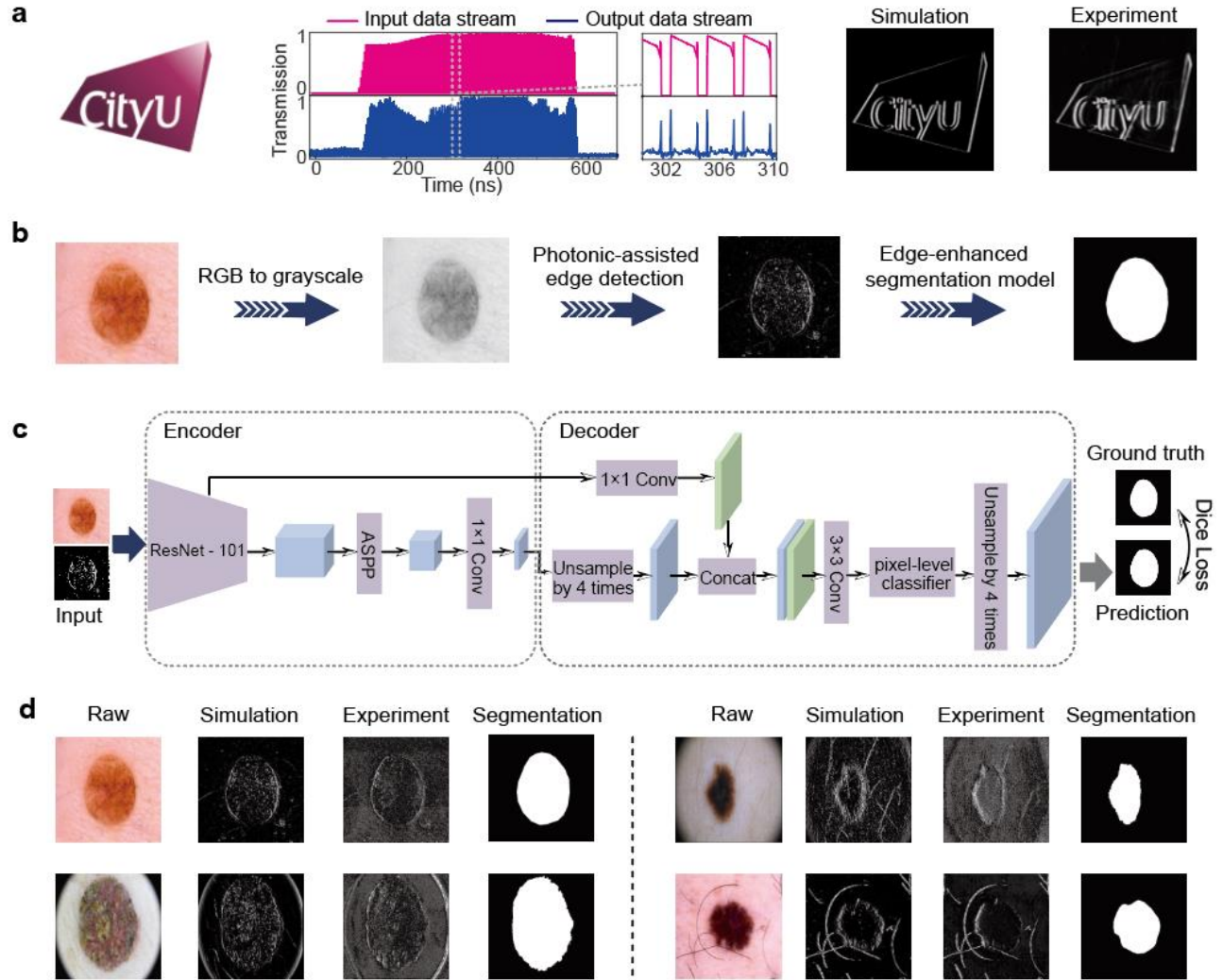**High-speed photonic-assisted image segmentation system**

Finally, we show our high-speed LN photonic processing engine could enable applications beyond traditional MWP-related scenarios. As an example, we realize a photonic-assisted image edge detector for segmentation of medical images, which can provide quantitative analysis to help clinicians conduct accurate disease diagnosis and treatment. The extraction of image edge features is realized by performing field-to-field differentiation operations on a time-domain data stream serialized from 2D images (see methods). We first showcase the power of our edge-feature detector by feeding the system with a 250×250-pixel 'CityU' logo, serialized as a 92 GSa/s data stream. The temporal differentiation and edge detection functions are performed "on-the-fly" within a short time ($250 \times 250 \times \frac{1}{92 \text{ GSa/s}} = 679$ ns) and captured by a real-time oscilloscope. We de-multiplex the captured time-series data back into matrix format to form the reconstructed image, showing clearly resolved edge features with 95.51% accuracy compared with the simulated results (Fig. 4a).

Importantly, the demonstrated image processor is three orders of magnitude faster and consumes lower power than performing traditional algorithms in an electronic computer (see Methods). The processing speed is currently limited by the sampling rate of our AWG and could be readily increased to at least 200 GSa/s considering the large analog bandwidth of our EO modulators deep into the millimeter-wave band [33].

We then plug our high-speed photonic-assisted image edge detector into a deep convolution neutral network (DCNN)-based image segmentation model for outlining the boundaries of melanoma lesion in medical diagnostic images with superior processing speed, power consumption and accuracy. When processing complex and often low-contrast medical images, the fuzzy boundaries between abnormal and normal regions could lead to predictions with compromised accuracies. This situation could be substantially improved by feeding the DCNN with edge-detected information instead of original images, which can be integrated into an

arbitrary encoder-decoder architecture in an end-to-end way for medical image segmentation process [45]. Figure 4b-c illustrates the flow diagram and working principle of the proposed edge-enhanced DCNN segmentation model that intakes raw RGB images and outputs segmentation results (see methods). To optimize the segmentation model, we first train the model with concatenated dermoscope images and the corresponding melanoma edge information derived from simulated differentiation, emphasizing the representations around melanoma lesion boundaries. Based on the optimized model, the test dermoscope images are concatenated with experimentally extracted lesion edge information to generate the melanoma region prediction. Figure 4d shows the original melanoma lesion images captured from dermoscope, simulated and experimentally measured edge features, as well as the lesion regions segmented by our model, respectively. The tested average segmentation accuracy of our edge-facilitated model is 95.44 %, proving the effectiveness of the proposed photonic-assisted segmentation model. Most importantly, the demonstrated LN photonic-assisted image edge detector features much higher computation speed and lower power consumption compared with traditional electronics (see methods), which will pave the path for high-complexity, high-throughput and real-time medical diagnosis tasks. The functional toolbox of our LN photonic image processing engine could be further expanded and parallelized leveraging the excellent scalability of our platform, leading to more advanced functions like matrix multiplication [10] and enabling a variety of future photonics-enabled AI and computer vision technologies.

Fig. 4. High-speed photonic-assisted medical image segmentation. a. Photonic-assisted image edge detection of a 250 ×250-pixel 'CityU' logo. **b.** Flow diagram of the photonic-assisted image segmentation model. The edge features of melanoma legion images are extracted by our LN-based image-edge detector and passed through a DCNN-based segmentation model to obtain the lesion segmentation results. **c.** Schematic diagram of the image segmentation model. **d.** Examples of melanoma lesion segmentation results showing original dermoscope images, simulated and experimentally extracted edge features, as well as the lesion regions segmented by our model, respectively.

Discussions

In summary, we have designed, fabricated and demonstrated a high-fidelity and low-power-consumption integrated microwave signal processing system that performs temporal integration and differentiation operations for high-speed electronic signals up to 92 GSa/s, enabling a variety of applications including ODE solving, UWB signal generation and edge detection of images. In particular, our photonic-assisted image segmentation model proves to be more powerful and efficient for disease diagnosis tasks, bringing exciting

16

opportunities for intersections between integrated MWP technology and medical diagnosis. The performance of the current system can be further improved, by utilizing microresonators with even higher Q factors [39] to prolong the integration time to nanoseconds [6], and MZIs with larger FSR to further increase the bandwidth of differentiation operation. The reconfigurability and programmability of our LN-based on-chip MWP signal processing system could be further enhanced by equipping thermo-optic or EO tuning sections on the processing blocks to allow real-time switching among processing functions and active tuning of the processing bandwidth for task-oriented applications [6,7,9]. Adoption of multiple input/output ports with controllable (de-)multiplexers could enable parallel linear processing [50] and space-division multiplexing [51]. Importantly, our demonstrated MWP system is highly compatible with other high-performance photonic components available on the integrated LN platform, such as microcombs [52], frequency shifters [41], and true delay lines [42], which could be further integrated towards even more advanced MWP functionalities. Meanwhile, we expect other components of the MWP system, such as low-noise laser sources, high-power handling PDs, electronic integrated circuits, and microwave amplifiers, could be assembled on the LN platform through heterogeneous integration schemes, leading to highly compact, cost-effective and high-performance integrated MWP systems for next-generation communications and information technologies.

Methods

Design and fabrication of the devices:

Devices are fabricated from a commercially available x-cut LNOI wafer (NANOLN), with a 500-nm LN thin film, a 2-μm buried SiO_2 layer, and a 500-μm silicon substrate. SiO_2 is first deposited on the surface of a 4-inch LNOI wafer as etching hard mask using plasma-enhanced chemical vapor deposition (PECVD). Optical waveguides, MZIs and microring resonators are then patterned on the entire wafer using an ASML UV Stepper lithography system (NFF, HKUST) die by die (1.5 cm×1.5 cm) with a resolution of 400 nm. Next, the exposed resist patterns are transferred first to the SiO_2 layer using a standard fluorine-based dry etching process, and then to the LN device layer using an optimized Ar+ based inductively-coupled plasma (ICP) reactive-ion etching process. The LN etch depth is ~ 250 nm, leaving a 250-nm-thick slab. After removal of the residual SiO_2 mask and redeposition, a second stepper lithography, metal evaporation and lift-off process are used to fabricate the microwave electrodes. The positive and negative electrodes are spaced by a gap of 5 μm to ensure strong EO coupling while minimizing metal-induced optical losses. Finally, chips are carefully cleaved for end-fire optical coupling with coupling loss ~ 4 dB per facet.

Characterization of the building blocks for MWP signal processing:

More details are presented here for the LN building blocks shown in Fig. 1. For optical characterizations, a continuous-wave pump laser (Santec TSL-510) is sent to the devices under test using a lensed fiber after a polarization controller to ensure TE polarization. The output optical signal is collected using a second lensed fiber and sent to a 125-MHz PD (New Focus 1811) for low-frequency measurements. The optical transmission of the racetrack resonator (waveguide width ~ 2 μm) is fitted by a Lorentzian function, with a loaded Q factor > 4 million, indicating a corresponding propagation loss of below 0.1 dB/cm.

For the on-chip MZI modulator, the small-signal EO S_{21} response is measured by injecting small RF signals from a vector network analyzer (VNA, Keysight N4373E) into the modulation electrodes via a high-speed probe (GGB industries) and monitoring the output signals captured by a high-speed PD (New Focus 1544) at various frequencies at the other port of the VNA. RF cable losses, probe loss and PD response are calibrated and de-embedded from the measured S_{21} responses, with typical 3-dB EO bandwidths > 50 GHz. Higher bandwidth could be obtained by micro-structured electrodes [53]. The measured low-frequency half-wave voltage (V_π) is 2.6 V for a modulation length of 1 cm, corresponding to a voltage–length product of 2.6 V·cm. For the on-chip phase modulator, an optical frequency comb consisting of 15 comb lines could be obtained by driving the modulator with a strong 18-GHz microwave signal with an amplified power of 630 mW, corresponding to a total acquired phase shift of ~ 1.05π. The comb spectrum is measured by an optical spectrum analyzer (OSA, Yokogawa AQ6370).

To implement temporal integration, an over-coupled add-drop racetrack resonator with free spectral range (FSR) ~ 80 GHz is fabricated, with a loaded Q-factor ~ 9×10^5 and near-unity on-resonance transmission measured at the drop port. For second-order integration, two cascaded racetrack resonators with different FSRs (80 GHz and 82 GHz) are designed to align the two resonance peaks via Vernier effect. The envelop FSR is measured to be 26.24 nm, which is in line with the design value. For temporal differentiation, the asymmetrical MZI and cascaded MZIs are designed with FSR ~ 50 GHz to provide a reasonable balance between operation bandwidth and differentiation slope efficiency. The spiral waveguides are designed with a minimum radius of curvature of ~ 100 μm to minimize the footprint and limit excessive radiation loss.

Principles of the microring-based MWP temporal integrator and ODE solver:

More details are presented here for the principles of microring-based temporal integrator and ODE solver. The integration results are represented in optical intensity changes on top of a DC intensity component when the amplitude modulator is biased at the quadrature point, which are captured by an AC-coupled high-speed PD. The optical field right after amplitude modulation can be expressed as:

$$E_{in}(t) = E_0 e^{j\omega_0 t} \cos\left[\beta x(t) + \varphi_0\right] \tag{1}$$

where β is the modulation index defined as $\pi V_p/V_\pi$, V_p is the peak voltage applied to the driving electrodes, E_0 is the input electric field amplitude, φ_0 is the bias phase of the amplitude modulator $-\pi/4$, ω_0 is the optical

18

carrier frequency and $x(t)$ is the normalized input microwave signal. Under small signal modulation ($\beta <<1$), the expression can be simplified as:

$$E_{in}(t) \approx \frac{\sqrt{2}}{2} E_0 e^{j\omega_0 t} \left[\beta x(t) + 1 \right] \tag{2}$$

After Fourier transformation, the input signal can be rewritten in frequency domain as:

$$E_{in}(\omega) = \mathcal{F}\left[\frac{\sqrt{2}}{2} \beta E_0 e^{j\omega_0 t} x(t) \right] + \frac{\sqrt{2}}{2} E_0 \delta(\omega - \omega_0) \tag{3}$$

After going through the integrator/ODE solver $\left[H(\omega) = \frac{1}{j(\omega - \omega_0) + k} \right]$, the output signal can be written as:

$$E_{out}(\omega) = E_{in}(\omega) H(\omega) = \frac{\mathcal{F}\left[\frac{\sqrt{2}}{2} \beta E_0 e^{j\omega_0 t} x(t) \right]}{j(\omega - \omega_0) + k} + \frac{\frac{\sqrt{2}}{2} E_0 \delta(\omega - \omega_0)}{j(\omega - \omega_0) + k} \tag{4}$$

When performing integration operations, we use microring resonators with ultrahigh Q-factors ($k \approx 0$), such that the output signal after inverse Fourier transformation back to the time domain is:

$$E_{out}(t) = F^{-1}\left[E_{out}(\omega) \right] \approx \mathcal{F}^{-1}\{ \frac{\mathcal{F}\left[\frac{\sqrt{2}}{2} \beta E_0 e^{j\omega_0 t} x(t) \right]}{j(\omega - \omega_0)} + \frac{\frac{\sqrt{2}}{2} E_0 \delta(\omega - \omega_0)}{k} \}$$

$$= \frac{\sqrt{2}}{2} \beta E_0 e^{j\omega_0 t} \int x(t) dt + \frac{\sqrt{2}}{2} e^{j\omega_0 t} \frac{E_0}{k} \tag{5}$$

The output current of the PD could then be written as:

$$I_{out}(t) \propto \Re |E_{out}(t)|^2 = \frac{\Re E_0^2}{2k^2} + \frac{1}{2} \Re \beta^2 E_0^2 \left[\int x(t) dt \right]^2 + \frac{\Re \beta E_0^2}{k} \int x(t) dt$$

$$\approx \frac{\Re \beta E_0^2}{k} \int x(t) dt \tag{6}$$

where $\Re$ is the responsivity of the PD. Here the AC-coupled PD only responds to the third term in Eq. (6) since the first term is time-invariant and the second term is small for small signals. Therefore, the output signal of the PD directly corresponds to the integration result [$I_{out}(t) \propto \int x(t) dt$], which is generally the case for all field-to-intensity integration and differentiation results in this work.

On the other hand, when the internal decay loss of the ring resonator is non-negligible ($k \neq 0$), the output signal can be rewritten as:

$$E_{out}(t) = F^{-1}\left[E_{out}(\omega) \right] \approx \mathcal{F}^{-1}\{ \frac{\mathcal{F}\left[\frac{\sqrt{2}}{2} \beta E_0 e^{j\omega_0 t} x(t) \right]}{j(\omega - \omega_0) + k} + \frac{\frac{\sqrt{2}}{2} E_0 \delta(\omega - \omega_0)}{k} \}$$

$$= \frac{\sqrt{2}}{2} \beta E_0 e^{j\omega_0 t} e^{-kt} \int e^{kt} x(t) dt + \frac{\sqrt{2}}{2} e^{j\omega_0 t} \frac{E_0}{k} \tag{7}$$

The output PD signal is then:

$$I_{out}(t) \propto \Re |E_{out}(t)|^2 \approx \frac{\Re \beta E_0^2}{k} e^{-kt} \int e^{kt} x(t) dt \propto e^{-kt} \int e^{kt} x(t) dt \tag{8}$$

which is the solution of the first-order ODE solved in this work.

Principles of the MZI-based MWP temporal differentiators:

More details are presented here for the temporal differentiator. After loading the electronic signal into LN phase modulator, the electric field can be expressed as:

$$E_{in}(t) = E_0 e^{j\omega_0 t + j\beta x(t)} \tag{9}$$

where β is the modulation index defined as $\pi V_p/V_\pi$. Here V_π corresponds to the half-wave voltage of a phase modulator. We achieve field-to-field differentiation when the MZI-based differentiator is biased at the null point with a frequency-domain transfer function of $j(\omega - \omega_0)$. The output signal in frequency domain can then be written as:

$$E_{out}(\omega) = E_{in}(\omega)H(\omega) = j(\omega - \omega_0)E_{in}(\omega) \tag{10}$$

Converting the output signal back into time domain through an inverse Fourier transformation yield:

$$E_{out}(t) = \mathcal{F}^{-1}\left[E_{out}(\omega)\right] = \frac{dE_{in}(t)}{dt} - j\omega_0 E_{in}(t)$$

$$= j\beta \frac{dx(t)}{dt} E_0 e^{j\omega_0 t + j\beta x(t)} \tag{11}$$

Here since the output differentiation result is represented as optical field without a constant DC component, the PD picks up the output intensity which represents the square of the calculated derivative:

$$I_{out}(t) \propto \Re|E_{out}(t)|^2 = \Re\beta^2 E_0^2 \left[\frac{dx(t)}{dt}\right]^2 \tag{12}$$

As a result, all measured signals for field-to-field differentiation processes in this work are positive only.

On the other hand, we achieve field-to-intensity differentiation when biasing the MZI at the quadrature point. For simplicity, we assume the slope of the transfer function to be 1, in this case the output signal in frequency domain can be written as:

$$E_{out}(\omega) = E_{in}(\omega)H(\omega) = (\omega - \omega_n)E_{in}(\omega) \tag{13}$$

where ω_n is the null point of the MZI-based differentiator. Then convert the output signal back into time domain by an inverse Fourier transformation:

$$E_{out}(t) = \mathcal{F}^{-1}\left[E_{out}(\omega)\right] = -j\frac{dE_{in}(t)}{dt} - \omega_n E_{in}(t)$$

$$= \left[(\omega_0 - \omega_n) + \beta\frac{dx(t)}{dt}\right]E_{in}(t) \tag{14}$$

The output intensity captured by the PD is then:

$$I_{out}(t) \propto \Re|E_{out}(t)|^2 = \Re\left[(\omega_0 - \omega_n) + \beta\frac{dx(t)}{dt}\right]^2 E_0^2$$

$$= \Re E_0^2 \left\{(\omega_0 - \omega_n)^2 + \beta^2\left[\frac{dx(t)}{dt}\right]^2 + 2\beta(\omega_0 - \omega_n)\frac{dx(t)}{dt}\right\} \tag{15}$$

where only the third term is effectively picked up by the AC-coupled PD under small signal modulation ($\beta << 1$), similar to the field-to-intensity integration case. Therefore, the expression can be simplified as:

$$I_{out}(t) \approx 2\beta\Re E_0^2(\omega_0 - \omega_n)\frac{dx(t)}{dt} \tag{16}$$

Methodologies of the integration, differentiation and image edge-detection experiments:

In our experiment, different analog signals are pre-encoded by an arbitrary waveform generation (AWG, Keysight M8196A) and loaded into the LN-based on-chip MWP system using the same high-speed photonic chip measurement setup as discussed before. Continuous wave optical carrier from the tunable laser is first amplified using an EDFA (JDS Uniphase, C-band) before sending into the chip thanks to the high power-handling capability of our LN devices, therefore minimizing the additional noise from EDFA when amplifying

small signals. The output light of the LN chip is detected by a photoreceiver (New Focus 1544) and sent to a high-speed oscilloscope (DSO-X 91604A) for signal analysis. For the temporal integrator experiment, the analog signals are combined with a DC bias voltage through a bias-tee to keep the MZI modulator at the quadrature point. The laser wavelength is fine tuned to align with the corresponding operating wavelengths of the integrators and differentiators. For UWB generation, the output spectrum is measured using an RF spectrum analyzer (R&S, FSW43) from 100 MHz to 15 GHz.

The photonic-assisted image edge detector is based on the field-to-field differentiator, which benefits from the direct intensity detection at the PD. The image information is encoded into a time-domain signal by serializing the pixels into a sequence of pulses and output at a highest sampling rate of 92 GSa/s using the AWG. Note that the "broadened" edges in the experimental results are caused by the relatively low and unmatched sampling rate of our oscilloscope (40 GSa/s). To achieve the best edge detection results in the medical image processing experiments, we lower the sampling rate to 40 GSa/s to match with the sampling rate of the oscilloscope.

**Image segmentation model and training process:**

More details are presented here for the principle of image segmentation model shown in Fig. 4c. We follow the network structure of DeepLabv3+ [54], which is composed of an encoder and a decoder. The former incorporates a ResNet101[55], Atrous Spatial Pyramid Pooling (ASPP) [54], and a 1×1 convolutional layer (conv) to extract deep features. The latter aims to recover the original image resolution and produce segmentation results. To optimize the segmentation model, we first collect simulated edge data for each medical image, which are concatenated together to feed into the encoder of the segmentation model, emphasizing the representations around melanoma boundaries. The deep features extracted from the encoder are then bilinearly up-sampled by a factor of 4 and concatenated with the corresponding low-level features from the ResNet101 backbone, which can preserve the detailed texture information, such as edges. These concatenated feature maps are further passed through a 3×3 convolutional layer, followed by a pixel-level classifier and a bilinear up-sampling operator, thereby deriving segmentation predictions. The obtained predictions are constrained by the dice loss [56]. By minimizing the dice loss, the optimized model has the ability to outline melanoma lesions given any test dermoscope images.

In implementation, we firstly construct a training dataset with 1000 dermoscope images [57], together with the corresponding simulated edge information and melanoma segmentation ground truths. Each dermoscope image is concatenated with its simulated edge data, and then the concatenated data are passed through the cascaded encoder and decode of the segmentation model, obtaining segmentation prediction from the output of the decoder. The resulting prediction is supervised by the corresponding segmentation ground truth through minimizing the computed dice loss. Our method is implemented with the PyTorch library. The input images are uniformly resized to 250×250 for training. The stochastic gradient descent optimizer is adopted with an initial learning rate of 10^{-5} for the pre-trained encoder and 10^{-4} for the rest trainable parameters within the segmentation model with random initialization. Polynomial learning rate scheduling is adopted with the power of 0.9. We choose a batch size of 8 and the maximum epoch number of 200 to guarantee the convergence of training.

Error analysis and performance evaluation:

All error analyses in this work are performed by calculating the mean absolute error (MAE) between the experimentally measured results and the ideal ones within the differentiation/integration time. We model and analyze the errors mainly from four sources: *i*) The limited bandwidth of measurement devices. In our measurement setup, the 12-GHz PD does not faithfully capture the high-frequency components of the output signals, resulting in the distortion of output signal in time domain, as illustrated in Extended Data Fig. 1a in the case of a 30-ps Gaussian pulse. We expect the MAE to decrease from 15% to 3% if an ideal PD is used. *ii*) The possible drift of device operation points. Extended Data Fig. 1b demonstrates the simulated output result where the bias point for field-to-field differentiation drifts slightly by 3 MHz, which clearly exhibits an asymmetric doublet pulse for a 90-ps input Gaussian pulse. *iii*) The intrinsic signal distortion from AWG. Adopting the actual 800-ps super-Gaussian pulse from our AWG as input signal, the simulated differentiation

result shows pulses with different heights at the rising and falling edges in Extended Data Fig. 1c. Using an ideal signal generator, the MAE could drop from 3.5% to 1.5%. *iv*) The intrinsic processing bandwidths of the proposed integrator/differentiator devices. Taking a short 10-ps Gaussian pulse as an example (under the ideal test equipment), the pulse bandwidth is much broader than the FSRs of the ring-based integrator (80 GHz) or the MZI-based differentiator (50 GHz), leading to clear distortion of processing results shown in Extended Data Fig. 1d-e.
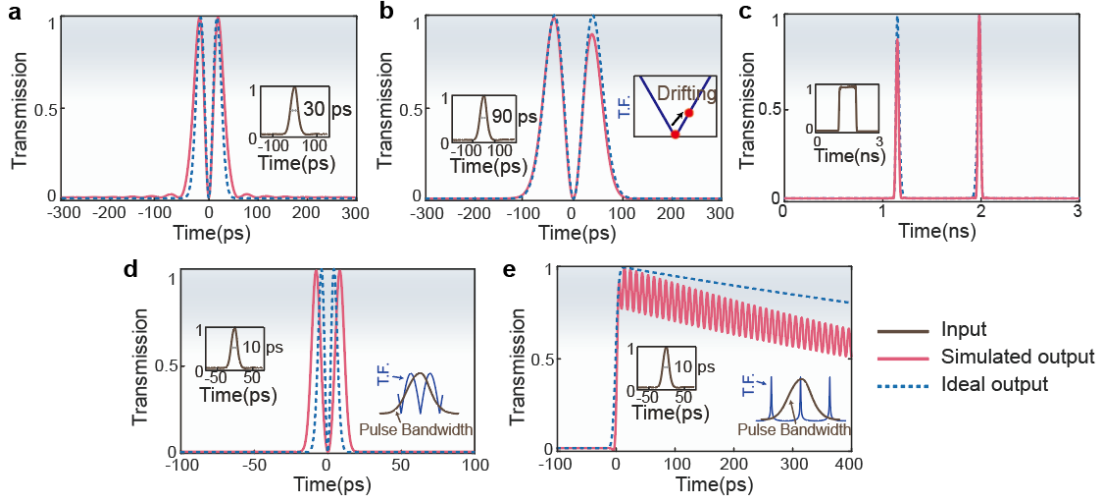
Extended Data Fig. 1. Error analyses based on simulated output signals with considerations of various practical limitations, including (a) limitation of equipment bandwidth, (b) drifting of device operation point, (c) intrinsic distortion of the input signals from AWG, as well as bandwidth limitations of the (d) MZI-based differentiator and (e) ring-based integrator. T.F., transfer function.

In real applications, the proposed high-speed microwave signal processor should enable accurate signal processing within broad bandwidths. To evaluate the error performance, the measured transfer functions of the integrator, differentiator and ODE solver are utilized for error analysis. The simulated MAE values of these functional devices (Extended Data Fig. 2) at different input signal bandwidths are analyzed by assuming ideal measured equipment (red curve) and our current equipment (green curve), respectively, consistent with our measured error performances (blue crosses and purple stars). Low computation errors of less than 10% (dash line) could be maintained within broad bandwidths of 1.5 ~ 40.7, 0.3 ~ 41.8 and 0 ~ 43.3 GHz for the integrator, differentiator and ODE solver, respectively. The lower operation frequency bound of the integrator is mainly limited by the discrepancy between the ideal and actual transfer functions near the resonance wavelength (Fig. 2c), whereas the lower bound of the differentiator is limited by non-ideal device transfer functions near the null point of the MZI (e.g. finite extinction ratios). The upper bounds of operation frequencies for all three devices are limited by the FSRs of corresponding ring resonators/MZIs, as discussed in Extended Data Fig. 1.
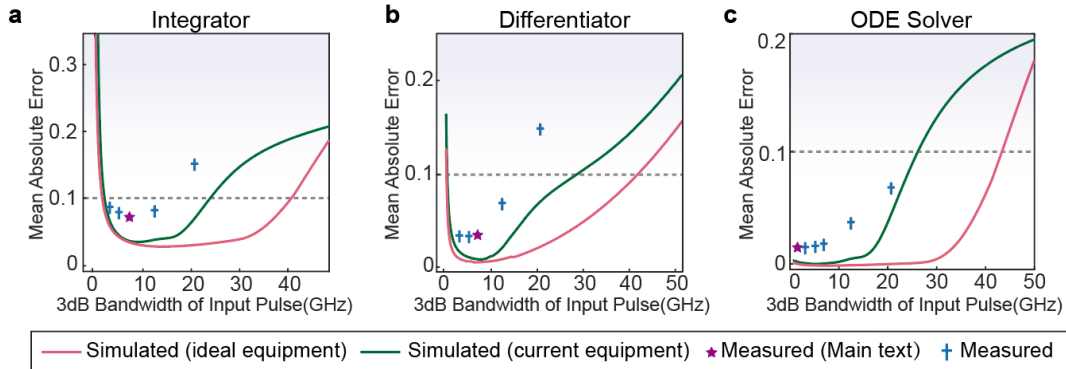
Extended Data Fig. 2. Simulated and measured mean absolute errors as functions of the input pulse bandwidth for (a) the temporal integrator, (b) the temporal differentiator, and (c) the ODE Solver.

Performance comparison with electronic computer-based algorithms and hardware

Extended Data Table 1 lists a detailed performance comparison between traditional electronics-based algorithms (including convolution-based and simple differentiation-based algorithms) and our photonic-assisted segmentation model. The performance metrics include raw lesion edge detection accuracy (from the edge detectors only, before DCNN), final segmentation accuracy (after DCNN), computation time, and energy consumption. The accuracies of lesion edge detection and segmentation are measured by dice coefficient. Extended Data Fig. 3 shows the raw edge detection results of an example lesion image using different processing methods, together with the ground truth. Our photonic edge detector shows a better raw edge detection accuracy (23.5%) than those of both convolution-based (18.1%) and differentiation-based (12.8%) algorithms, mainly because it picks up less false-positive details inside the lesion region. The final image segmentation accuracies are above 95% for all three methods but with drastically different processing time. For edge feature extraction of a 250×250-pixel image, our device consumes a total computation time of 679 ns, nearly three orders of magnitude faster than performing a traditional convolution algorithm on a generic personal computer (380 μs).

When estimating the power consumption of electronics-based edge detection, we realize the challenges of quantifying the exact power consumption of DSP at the chip level, and only provide a lower-bound estimation by calculating the power consumed on the basic multiplication and addition operations of the edge-detection algorithms [58]. The energy consumption could be estimated as:

$$E_{ele} = T \cdot M \cdot [N \cdot E_M + (N-1) \cdot E_A] + (T-1) \cdot M \cdot E_A \tag{17}$$

where T is the kernel number, which is typically 4 for a convolution algorithm and 2 for a differentiation algorithm. M is the image pixel number, which is 250×250 in this case. N is the kernel size, which is 9 for the convolution algorithm and 3 for the differentiation algorithm. We assume 7 nm CMOS node is used for DSP chips, with an energy consumption per multiplication operation $E_M \sim 486$ fJ/b and an energy consumption per addition operation $E_A \sim 60.8$ fJ/b [59]. Therefore, the estimated total energy consumption for convolution algorithm is ~ 1227 nJ and for differentiation algorithm is ~ 201 nJ.

For our photonic-assisted method, we estimate the total energy dissipation on our photonic chip by including the power consumptions of the pump laser, modulator, as well as PD. The electrical energy dissipated can be estimated as [36,58-60]:

$$E_{pho} = E_{laser} + E_{mod} + E_{PD} \tag{18}$$

where E_{laser} is the energy consumption from the pump laser, considering the optical power of 10 mW and total processing time of 679 ns, leading to $E_{laser} \sim 6.79$ nJ. E_{mod} is the energy consumption of the EO modulator, which intakes a driving peak voltage of $V_p = 500$ mV and consumes an average power consumption of $\frac{V_p^2}{2R} = 2.5$ mW, where $R = 50$ Ω is the load impedance of the modulator [36], leading to an E_{mod} of ~ 1.7 nJ within the processing time. E_{PD} is the energy consumption of the PD, which could be estimated as $\frac{\Re V_{bias} p_{rec}}{B}$ [60], where $\Re$ is the responsivity of the PD ~ 0.6 A/W, V_{bias} is the PD bias voltage ~ 3.3 V, p_{rec} is the received optical power ~ 1 mW, B is the information bit rate ~ 92 Gbit/s, leading to $E_{PD} \sim 1.34$ nJ. The total energy consumption of our photonic edge detector E_{pho} is therefore estimated to be ~ 9.8 nJ.
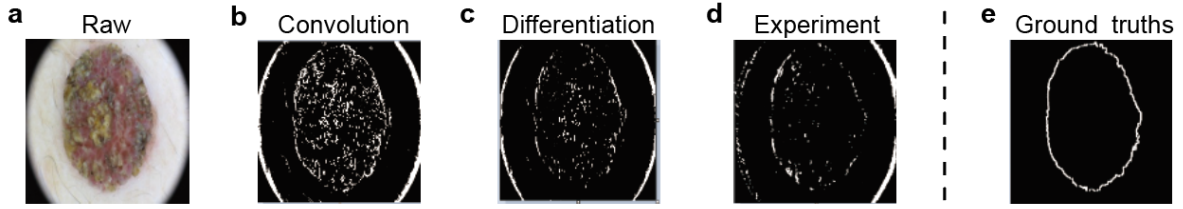
Extended Data Fig. 3. Raw edge-detection results of a representative melanoma lesion image **a.** using convolution **b**. and simple differentiation **c**. algorithms in electronic computers, our photonic-assisted edge detector **d**, and the ground truths **e**.

Extended Data Table. 1. Performance comparison with traditional electronics-based algorithms

	Differentiation algorithm	Convolution algorithm	This work
Raw lesion edge detection * †	12.831%	18.149%	23.509%
Segmentation accuracy*	95.602%	95.888%	95.437%
Computation time	120 μs	380 μs	0.679 μs
Energy consumption	201 nJ	1227 nJ	9.8 nJ

* Detection and segmentation accuracies are measured by dice coefficient.
† Raw detection accuracy right after edge detection algorithms, before entering DCNN.

Author contributions

H.F. and C.W. conceived the idea. H.F. designed and fabricated the wafer with the help of K.Z., Y.Z., Z.C. and W.S. T.G. and X.G. performed the numerical simulations. H.F. and T.G. carried out the measurement and analyzed the data with the help of X.G., S.Z. and Y.Z. H.F. prepared the manuscript with contribution from all authors. Y.Y. and C.W. supervised the project.

Conflict of interest.

The authors declare no conflicts of interest.

Data availability.

Data underlying the results presented in this paper are not publicly available at this time but may be obtained from the authors upon reasonable request.

References

1 Capmany, J. & Novak, D. Microwave photonics combines two worlds. Nat. Photon. 1, 319 (2007).
2 Marpaung, D., Yao, J. & Capmany, J. Integrated microwave photonics. Nat. Photon. 13, 80-90 (2019).
3 Shu, H. et al. Microcomb-driven silicon photonic systems. Nature 605, 457-463 (2022).
4 Fandiño, J. S., Muñoz, P., Doménech, D. & Capmany, J. A monolithic integrated photonic microwave filter. Nat. Photon. 11, 124-129 (2017).
5 Sancho, J. et al. Integrable microwave filter based on a photonic crystal delay line. Nat. Commun. 3, 1-9 (2012).
6 Liu, W. et al. A fully reconfigurable photonic integrated signal processor. Nat. Photon. 10, 190-195 (2016).
7 Pérez, D. et al. Multipurpose silicon photonics signal processor core. Nat. Commun. 8, 1-9 (2017).
8 Zhang, W. & Yao, J. Photonic integrated field-programmable disk array signal processor. Nat. Commun. 11, 1-9 (2020).
9 Zhang, W. & Yao, J. A fully reconfigurable waveguide Bragg grating for programmable photonic signal processing. Nat. Commun. 9, 1-9 (2018).
10 Feldmann, J. et al. Parallel convolutional processing using an integrated photonic tensor core. Nature 589, 52-58 (2021).
11 Xu, X. et al. 11 TOPS photonic convolutional accelerator for optical neural networks. Nature 589, 44-51 (2021).
12 Ilderem, V. The technology underpinning 5G. Nat. Electron. 3, 5-6 (2020).
13 Khan, M. H. et al. Ultrabroad-bandwidth arbitrary radiofrequency waveform generation with a silicon photonic chip-based spectral shaper. Nat. Photon. 4, 117-122 (2010).
14 Wang, J. et al. Reconfigurable radio-frequency arbitrary waveforms synthesized in a silicon photonic chip. Nat. Commun. 6, 1-8 (2015).
15 Zhu, C. et al. Silicon integrated microwave photonic beamformer. Optica 7, 1162-1170 (2020).
16 Tao, Y. et al. Fully On‑Chip Microwave Photonic Instantaneous Frequency Measurement System. Laser & Photonics Rev. 2200158 (2022).
17 Manolatou, C. & Lipson, M. All-optical silicon modulators based on carrier injection by two-photon absorption. J. Lightwave Technol. 24, 1433-1439 (2006).
18 Roeloffzen, C. G. et al. Silicon nitride microwave photonic circuits. Opt. Express 21, 22937-22961 (2013).
19 Zhuang, L., Roeloffzen, C. G., Hoekman, M., Boller, K.-J. & Lowery, A. J. Programmable photonic signal processor chip for radiofrequency applications. Optica 2, 854-859 (2015).

20 Dong, J. et al. Compact, flexible and versatile photonic differentiator using silicon Mach-Zehnder interferometers. Opt. Express 21, 7014-7024 (2013).

21 Liu, W., Zhang, W. & Yao, J. Silicon-based integrated tunable fractional order photonic temporal differentiators. J. Lightwave Technol. 35, 2487-2493 (2017).

22 Slavík, R. et al. Photonic temporal integrator for all-optical computing. Opt. Express 16, 18202-18214 (2008).

23 Xu, X. et al. Microcomb-based photonic RF signal processing. IEEE Photon. Technol. Lett. 31, 1854-1857 (2019).

24 Minasian, R. A., Chan, E. & Yi, X. Microwave photonic signal processing. Opt. Express 21, 22918-22936 (2013).

25 Park, Y., Azaña, J. & Slavík, R. Ultrafast all-optical first-and higher-order differentiators based on interferometers. Opt. Lett. 32, 710-712 (2007).

26 Ferrera, M. et al. On-chip CMOS-compatible all-optical integrator. Nat. Commun. 1, 1-5 (2010).

27 Li, M., Jeong, H.-S., Azaña, J. & Ahn, T.-J. 25-terahertz-bandwidth all-optical temporal differentiator. Opt. Express 20, 28273-28280 (2012).

28 Morton, P. A. et al. High-power, high-linearity, heterogeneously integrated III–V on Si MZI modulators for RF photonics systems. IEEE Photon. J. 11, 1-10 (2019).

29 Tran, M. A. et al. Extending the spectrum of fully integrated photonics to submicrometre wavelengths. Nature 610, 54-60 (2022).

30 Xiang, C. et al. Laser soliton microcombs heterogeneously integrated on silicon. Science 373, 99-103 (2021).

31 Boes, A. et al. Lithium niobate photonics: Unlocking the electromagnetic spectrum. Science 379, 4396 (2023).

32 Zhang, M., Wang, C., Kharel, P., Zhu, D. & Lončar, M. Integrated lithium niobate electro-optic modulators: when performance meets scalability. Optica 8, 652-667 (2021).

33 Zhang, Y. et al. Systematic investigation of millimeter-wave optic modulation performance in thin-film lithium niobate. Photonics Res. 10, 2380-2387 (2022).

34 Mercante, A. J. et al. Thin film lithium niobate electro-optic modulator with terahertz operating bandwidth. Opt. Express 26, 14810-14816 (2018).

35 He, M. et al. High-performance hybrid silicon and lithium niobate Mach–Zehnder modulators for 100 Gbit s− 1 and beyond. Nat. Photon. 13, 359-364 (2019).

36 Wang, C. et al. Integrated lithium niobate electro-optic modulators operating at CMOS-compatible voltages. Nature 562, 101-104 (2018).

37 Ahmed, A. N. R. et al. Subvolt electro-optical modulator on thin-film lithium niobate and silicon nitride hybrid platform. Opt. Lett. 45, 1112-1115 (2020).

38 Feng, H. et al. Ultra-high-linearity integrated lithium niobate electro-optic modulators. Photonics Res. 10, 2366-2373 (2022).

39 Zhang, M., Wang, C., Cheng, R., Shams-Ansari, A. & Lončar, M. Monolithic ultra-high-Q lithium niobate microring resonator. Optica 4, 1536-1537 (2017).

40 Escalé, M. R., Pohl, D., Sergeyev, A. & Grange, R. Extreme electro-optic tuning of Bragg mirrors integrated in lithium niobate nanowaveguides. Opt. Lett. 43, 1515-1518 (2018).

41 Hu, Y. et al. On-chip electro-optic frequency shifters and beam splitters. Nature 599, 587-593 (2021).

42 Zhou, J.-x. et al. Electro-optically switchable optical true delay lines of meter-scale lengths fabricated on lithium niobate on insulator using photolithography assisted chemo-mechanical etching. Chinese Phys. Lett. 37, 084201 (2020).

43 Luke, K. et al. Wafer-scale low-loss lithium niobate photonic integrated circuits. Opt. Express 28, 24452-24458 (2020).

44 Li, Z. et al. Tightly confining lithium niobate photonic integrated circuits and lasers. arXiv:2208.05556 (2022).

45 Zhang, M., Yu, F., Zhao, J., Zhang, L. & Li, Q. BEFD: boundary enhancement and feature denoising for vessel segmentation. International Conference on Medical Image Computing and Computer-Assisted Intervention, 775-785 (2020).

46 Hill, M. T. et al. A fast low-power optical memory based on coupled micro-ring lasers. Nature 432, 206-209 (2004).

47 Tan, S. et al. High-order all-optical differential equation solver based on microring resonators. Opt. Lett. 38, 3735-3738 (2013).

48 Yang, T. et al. All-optical differential equation solver with constant-coefficient tunable based on a single microring resonator. Scientific reports 4, 1-6 (2014).

49 Pan, S. & Yao, J. UWB-over-fiber communications: modulation and transmission. J. Lightwave Technol. 28, 2445-2455 (2010).

50 Perez, D. et al. Silicon photonics rectangular universal interferometer. Laser & Photonics Revi. 11, 1700219 (2017).

51 Wen, H. et al. Few-mode fibre-optic microwave photonic links. Light: Sci. & Appl. 6, 17021-17021 (2017).

52 Zhang, M. et al. Broadband electro-optic frequency comb generation in a lithium niobate microring resonator. Nature 568, 373-377 (2019).

53 Kharel, P., Reimer, C., Luke, K., He, L. & Zhang, M. Breaking voltage–bandwidth limits in integrated lithium niobate modulators using micro-structured electrodes. Optica 8, 357-363 (2021).

54 He, K., Zhang, X., Ren, S. & Sun, J. Deep residual learning for image recognition. Proceedings of the IEEE conference on computer vision and pattern recognition, 770-778 (2016).

55 Chen, L.-C., Zhu, Y., Papandreou, G., Schroff, F. & Adam, H. Encoder-decoder with atrous separable convolution for semantic image segmentation. Proceedings of the European conference on computer vision (ECCV), 801-818 (2018).

56 Milletari, F., Navab, N. & Ahmadi, S.-A. V-net: Fully convolutional neural networks for volumetric medical image segmentation. 2016 fourth international conference on 3D vision (3DV), 565-571 (2016).

57 Codella, N. C. et al. Skin lesion analysis toward melanoma detection. 2018 IEEE 15th international symposium on biomedical imaging (ISBI 2018), 168-172 (2018).

58 Wang, B., de Lima, T. F., Shastri, B. J., Prucnal, P. R. & Huang, C. Multi-Wavelength Photonic Neuromorphic Computing for Intra and Inter-Channel Distortion Compensations in WDM Optical Communication Systems. IEEE J. Sel. Top. Quant. Electron. 29, 1-12 (2022).

59 Huang, C. et al. A silicon photonic–electronic neural network for fibre nonlinearity compensation. Nat. Electron. 4, 837-844 (2021).

60 Huang, C. et al. High-capacity space-division multiplexing communications with silicon photonic blind source separation. J. Lightwave Technol. 40, 1617-1632 (2022).